Applied Catalysis B: Environmental 204 (2017) 335–345

Contents lists available at ScienceDirect

Applied Catalysis B: Environmental

journal homepage: www.elsevier.com/locate/apcatb

A surface modification resultant thermally oxidized porous g-C_3N_4 with enhanced photocatalytic hydrogen production

Liuqing Yang[a,b], Jianfeng Huang[a,**], Li Shi[b], Liyun Cao[a], Qing Yu[b], Yanni Jie[a], Jie Fei[a], Haibo Ouyang[a], Jinhua Ye[b,c,d,*]

[a] School of Materials Science and Engineering, Shaanxi University of Science and Technology, Weiyang, Xi'an, Shaanxi 710021, PR China
[b] International Center for Materials Nanoarchitectomics (WPI-MANA), National Institute for Materials Science (NIMS), 1-1 Namiki, Tsukuba, Ibaraki 305-0044, Japan
[c] TU-NIMS Joint Research Center, School of Materials Science and Engineering, Tianjin University, 92 Weijin Road, Nankai District, Tianjin 300072, PR China
[d] Collaborative Innovation Center of Chemical Science and Engineering (Tianjin), Tianjin 300072, PR China

ARTICLE INFO

Article history:
Received 12 August 2016
Received in revised form 19 October 2016
Accepted 22 November 2016
Available online 22 November 2016

Keywords:
Graphitic carbon nitride
Thermal oxidation
Porous structure
Photocatalytic hydrogen evolution

ABSTRACT

Thermally oxidized porous g-C_3N_4 was obtained by a facile oxidation approach and 1430.1 μmol g^{-1} h^{-1} average photocatalytic hydrogen evolution is achieved in 8 h under visible-light irradiation, which was 4.3 times as high as that of the pristine sample (334.3 μmol g^{-1} h^{-1}). It is found that this modified g-C_3N_4 presented both porous structure and intrinsic electronic/band structure modulation, resulting in larger specific surface area with more surface reaction sites, extended light absorption range for more effective visible-light utilization, up-shifted conduction band for stronger reducibility and more effective separation of photogenerated charge carriers, which are beneficial for improving photocatalytic hydrogen evolution activity.

© 2016 Elsevier B.V. All rights reserved.

1. Introduction

Graphitic carbon nitride (g-C_3N_4) is one of the most promising materials and plays a vital role in photoelectrochemical energy conversion and storage, including solar cells, batteries, catalysis, supercapacitors, sensors and so forth [1–4]. As its appropriate band gap corresponding to a visible light absorption, together with its thermal and chemical stability, g-C_3N_4 is particularly suitable for applications in photochemistry and photocatalysis [5–9]. g-C_3N_4 has the structure of multilayer conditionally "defect-free" networks mostly constituted by heptazine (tris-s-triazine C_6N_7) fragments and deviations of the composition leads to an increase in amount of structural defects and active centers, as a consequence, improve its photocatalytic properties [7]. For example, g-C_3N_4 has been applied as photocatalyst for aqueous contaminants decomposition [10,11], NO removal [12,13], CO_2 reduction [14–16], oxygen evolution [17–19] and hydrogen generation [20–26]. However, its inefficient utilization for visible-light and high recombination of photoexcited charge carriers (electron–hole) results in unsatisfactory photocatalytic performance. Various modifications have been developed to solve this problem, for instance, the integrate with conductive materials (e.g. graphene, carbon [11,12]) or cocatalysts (Co [18] and Ni [24], etc.), the coupling with some semiconductors (AgBr [11], TiO_2 [13] $BiVO_4$ [17] and CdS [25], etc.) and the introduction of heteroatoms. Within those methods, metal-free heteroatom doping (N, S, B, I, P, O) [16,17,27–42] is an effective strategy to increase visible light harvesting capability by modifying the texture, surface chemical properties and the electronic structure, as well as narrowing the band gap of g-C_3N_4. Therefore, it has been demonstrated that N [27], P [31–34], I [35,36] and O-doped [37–42] g-C_3N_4 have behaved excellent performance for photocatalytic hydrogen production from water splitting. Besides, the physicochemical properties of g-C_3N_4 strongly depend on not only the composition but also its morphology [7], and g-C_3N_4 with porous structure can exhibit an improved photocatalytic hydrogen production activity due to the large specific surface area and more active sites and adsorption sites [21,38,43]. However, most of the reported metal-free heteroatom-doped g-C_3N_4 materials did not process porous structure [27,28,31,34–36] or porous structures were obtained from hazardous and toxic reagents (H_2SO_4, HNO_3, H_2O_2 or H_2S) [32,33,37,38], thus an eco-friendly method is highly

* Corresponding author at: International Center for Materials Nanoarchitectomics (WPI-MANA), National Institute for Materials Science (NIMS), 1-1 Namiki,Tsukuba, Ibaraki 305-0044, Japan.
** Corresponding author at: School of Materials Science and Engineering, Shaanxi University of Science and Technology, Weiyang, Xi'an, Shaanxi 710021, PR China.
E-mail addresses: huangjf@sust.edu.cn (J. Huang), jinhua.ye@nims.go.jp (J. Ye).

http://dx.doi.org/10.1016/j.apcatb.2016.11.047
0926-3373/© 2016 Elsevier B.V. All rights reserved.

desirable. The integration of these two favorable characteristics (heteroatom introducing and the construction of porous structure) in g-C_3N_4 photocatalyst from a simple, eco-friendly and low-cost method for the scalable modification method is rarely realized and is expected to be powerful in achieving high photocatalytic activities.

Here, we report a facile surface modification method for g-C_3N_4 photocatalysts by a thermal oxidation procedure (heating in oxygen at a designated temperature) without any other chemicals. This modification method is favorable for eco-friendly scale-type industrial production. The resultant thermally oxidized g-C_3N_4 is lightweight and freestanding, and has a large specific surface area as well as good structural stability. In addition, the oxygen-containing group has been proved to be active, and O atoms possess superiority in low cost, nontoxicity, and abundance. The structural properties and photocatalytic performances of this modification resultant sample in water splitting were investigated in detail. Remarkably, the thermally oxidized g-C_3N_4 exhibits significantly improved performance compared with its pristine sample for photocatalytic hydrogen evolution under visible light and also presents excellent recycle properties. From SEM, TEM, N_2 adsorption-desorption, XPS, FT-IR, XRD, Zeta potential, optical and phtotchemical analysis, the improved photocatalytic activity of this thermally oxidized porous g-C_3N_4 could be attributed to the synergistic effects of larger specific surface area, enhanced reduction power, improved electron transport ability and prolonged lifetime of charge carriers.

2. Experimental procedures

2.1. Synthesis of the samples

The pristine g-C_3N_4 was prepared by heating melamine at 550 °C in nitrogen for 4 h at 5 °C/min. And the thermally oxidized porous g-C_3N_4 was prepared by heating the pristine sample at a designated temperature (480, 510, 530, 540 and 550 °C) in oxygen for 30 min at 5 °C/min. Then for comparison the non-oxidized porous g-C_3N_4 was prepared by heating the pristine sample at 530 °C in argon for 30 min at 5 °C/min.

2.2. Preparation of g-C_3N_4 photoanodes

Clean indium tin oxide (ITO) glass was first obtained by sequentially washing with acetone, distilled water, and ethanol in an ultrasonic cleaner for 30 min. Then, 1.0 mg photocatalyst was well dispersed in 0.5 ml isopropanol containing 10 μl nafion and stayed in an ultrasonic cleaner for 30 min. Subsequently, all the above suspension was deposited dropwise by using a pipette onto the surface of an ITO glass with exposed 1×1 cm^2 area uniformly. After drying overnight in an oven, the electrodes were sintered at 200 °C in N_2 for 2 h to improve adhesion. The loading mass is about 1 mg/cm^2. The boundary of ITO glass was protected using transparent tape. The photocurrent measurements were carried out at 0.6 V (vs. Ag/AgCl).

2.3. Characterization

Morphology of the samples was characterized by a field emission scanning electron microscope (SEM, S4800, Hitachi Co., Japan). Nitrogen adsorption-desorption isotherms and pore size distributions of samples were measured using a nitrogen physisorption surface area analyzer (BEL Japan INC., Japan) at 77 K. Compositions, chemical state and valence band position of the samples were recorded on an X-ray photoelectron spectroscopy (XPS, PHI Quantera SXM, ULVAC-PHI Inc., Japan). Fourier transform infrared spectra (FT-IR) were recorded using an FT-IR spectrometer (Thermoscientific Nicolet 4700). Crystal structure of the samples was determined by an X-ray diffractometer (XRD, D/max-2200, Rigaku) with Cu Kα radiation (λ = 0.15418 nm). Zeta potential distributions of samples in pure water were recorded on an ELSZ-2000 (Otusuta Electronics). The photoluminescence (PL) spectra of samples were recorded on a spectrofluorometer (JASCO FP-6500). Time-resolved fluorescence (TRF) spectra of samples were detected by a fluorescence spectrofluorometer (Quantaurus-Tau, C11367, HAMAMATSU) under the 365 nm laser excitation at room temperature. Photocurrent response, electrochemistry impedance spectroscopy (EIS) and Mott-Schottky measurements were performed with a CHI electrochemical analyser (ALS/CH model 650A) using a standard three-electrode mode with 0.5 M Na_2SO_4 (pH 6.8) solution as the electrolyte, Ag/AgCl (saturated KCl) as the reference electrode and a Pt sheet as the counter electrode. The cleaned indium tin oxide (ITO) deposited with samples were fabricated respectively as photoanodes. The simulated sunlight was obtained using an AM 1.5 solar simulator (WXS-80C-3 AM 1.5G) with a light intensity of 0.1 W/cm^2. The photocurrent response of the photocatalysts as light on and off was measured with 0.6 V bias voltage. The MS measurements were carried out in the dark at the frequency of 500, 1000 and 1500 Hz, respectively. UV–vis diffuse reflectance spectra (DRS) were performed with an UV–vis spectrophotometer (Shimadzu, UV-2600) with $BaSO_4$ as the reflectance standard reference. Electron spin resonance (ESR) characterization was carried out using a JEOL JES-FA-200 at room temperature and the spectral parameters are shown in below: centre field = 321 mT, sweep width = 7.5 mT, microwave frequency = 8.99 GHz, modulation frequency = 100 KHz and power = 2 mW.

2.4. Photocatalytic H_2 production activity

Reactions were carried out in a Pyrex top-irradiation reaction vessel connected to a glass closed gas circulation system. H_2-production half reaction was performed by dispersing 50 mg of catalyst powder in an aqueous solution (280 ml) containing triethanolamine (10 vol.%) as a sacrificial electron donor. 3 wt% Pt was photodeposited on the catalysts using H_2PtCl_6 dissolved in the reactant solution. The reactant solution was evacuated several times to remove air completely prior to irradiation under a 300 W Xe lamp with a 420 nm cut-off filter (λ > 420 nm) as the light source. The powder density is 562.89 mW/cm^2. The temperature of the reactant solution is about 25 °C. The gas evolution in the reaction system were sampled and measured with a gas chromatograph (GC-14B, Shimadzu) equipped with a flame ionization detector (FID) according to the standard curves. The contents of H_2 were measured with an online gas chromatograph (GC-8A, Shimadzu) with a TCD detector according to the standard curve.

3. Results and discussion

3.1. Morphology analysis

The thermally oxidized g-C_3N_4 was prepared by heating the pristine g-C_3N_4 in pure oxygen atmosphere at a designated temperature for 30 min. It should be noted that oxidation level of g-C_3N_4 depends on the heating temperature and heating period. The heating temperature for preparing thermally oxidized g-C_3N_4 ranges from 480 to 550 °C. The C/N molar ratio and concentration of O atom increase with the increased reaction temperature (Supplementary Table S1). Fig. 1 shows the scanning electron microscope (SEM) images of the pristine and O_2 treated g-C_3N_4. It can be seen that the pristine g-C_3N_4 sample displays the typical stacked lamellar structure and slate-like morphology (Fig. 1). After O_2 treatment, the surfaces of resultant samples have been corroded and appear as irregular porous structures (Fig. 1). The diameters of pores range from several nanometers to several hundred nanometers. The

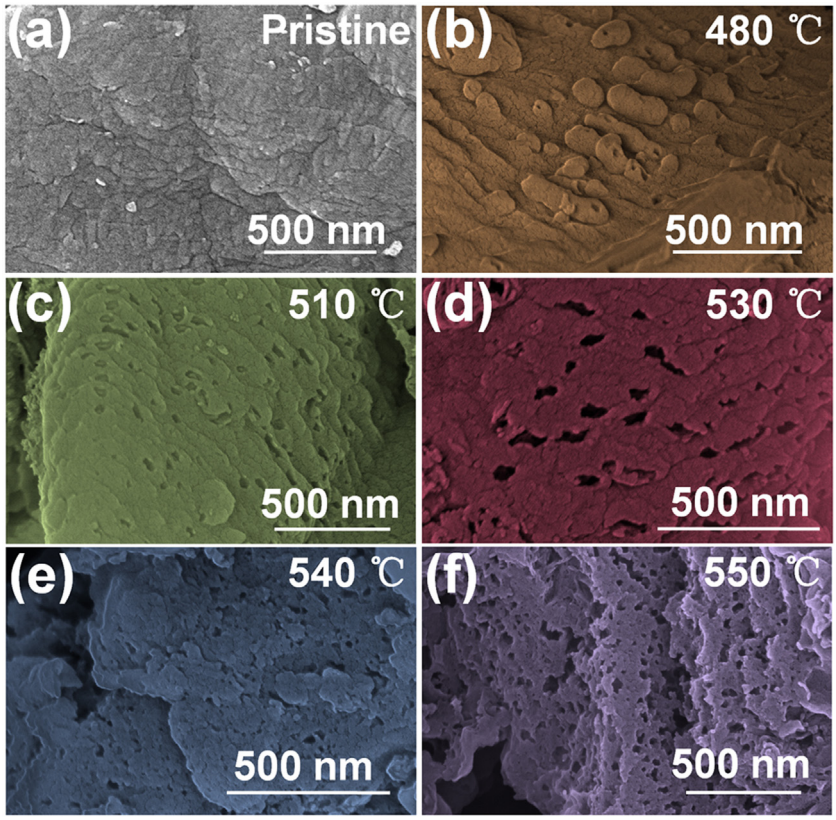

Fig. 1. SEM images of the pristine and the thermally oxidized g-C_3N_4 samples heated in oxygen 30 min at different temperatures: (a) pristine, (b) 480 °C, (c) 510 °C, (d) 530 °C, (e) 540 °C and (f) 550 °C.

transmission electron microscopy (TEM) images, as shown in Fig. 2, further confirm that the thermally oxidized g-C_3N_4 show porous structure, which is consistent with the SEM observation. In addition, the SEM and TEM images show that the pore volume increases with the increase of reaction temperature.

3.2. Surface area and chemical states analysis

Fig. 3 illustrates the N_2 adsorption-desorption isotherms and pore size distribution curves of pristine and thermally oxidized porous g-C_3N_4. The BET specific surface areas (S_{BET}) determined for the thermally oxidized g-C_3N_4 samples at 480 °C, 510 °C, 530 °C, 540 °C and 550 °C are 12.14, 15.60, 24.70, 28.51 and 67.70 $m^2\,g^{-1}$, respectively, which are higher than that of the pristine (9.56 $m^2\,g^{-1}$). Correspondingly, thermally oxidized g-C_3N_4 possess much larger pore volumes (0.04, 0.05, 0.06, 0.07 and 0.15 $cm^3\,g^{-1}$) compared to the pristine g-C_3N_4 (0.02 $cm^3\,g^{-1}$). The much higher BET surface area and pore volumes of thermally oxidized g-C_3N_4 may result from a large number of pores. Further insight into the pore structure of samples was revealed by the pore size distribution curves (Fig. 3, inset). The pore size distribution curves indicate that the thermally oxidized g-C_3N_4 are rich in pores of size between 1 and 20 nm (the pore at ≈4 nm is an artifact [44]), which proves that the micro/mesoporous structure of thermally oxidized g-C_3N_4 was well-developed. The N_2 adsorption-desorption isotherms for all the samples heated at different temperatures were similar and showed a type IV with H3 hysteresis loops. The BET surface areas increase with the rise of reaction temperature, which is consistent with the SEM and TEM observations, meaning that more pores are generated at higher reaction temperature. Such a dramatically increased BET surface area and micro/mesoporous structure of thermally oxidized g-C_3N_4 are expected to provide more exposed active sites for reactants, which should be more favorable for photocatalysis [37,38].

The formation of abundant pores on the surface of g-C_3N_4 is probably due to the oxidation by oxygen. Direct evidence of the oxidation coming from the formation of O-containing species on g-C_3N_4 surface is determined by X-ray photoelectron spectroscopy (XPS). As compared in Fig. 4, XPS survey spectra of all samples contain three sharp peaks at around 288, 398, and 532 eV, which are assigned to C 1s, N 1s, and O 1 s signals [37–41]. This indicates that the composition and chemical state of g-C_3N_4 are largely retained after oxygen etching at high temperature. C 1 s high-resolution spectra (Fig. 4b) show that, there are three kinds of carbon species in the thermally oxidized porous g-C_3N_4 samples. The core levels at 284.6 eV is from C(sp^2)-C(sp^2) in graphitic carbon species [22], around 287.7 eV is assigned to C atoms attached to N inside the aromatic ring (N=C—$(N)_2$) [45,46], and 289.0 eV is for C—O [37], respectively. Remarkably, the intensity of the peak at 289.0 eV increases with the increase of treating temperature, suggesting the involvement of the carboxylate groups by heating in oxygen at the temperature from 480 °C to 550 °C. Trace amount of C—O species was also detected in pristine g-C_3N_4, presumably due to surface contamination from calcination [47]. It is reasonable to notice that there exists trace amount of O_2 in the precursor melamine. Therefore, thermal decomposition of the melamine would produce trace amount of C—O species even in the N_2 atmosphere. Additionally, this 289.0 eV peak at pristine g-C_3N_4 is rather weak, thus the content of the C—O species from surface contamination should be very low [47]. Fig. 4c shows O 1 s high-resolution spectra of the pristine and thermally oxidized porous g-C_3N_4 samples. The O XPS spectra of pristine g-C_3N_4 can be deconvoluted into three peaks. The peaks at 534.0, 532.3 and 531.6 eV are for absorbed O_2, H_2O and C—O species, respectively [41,48]. Further treatment of the

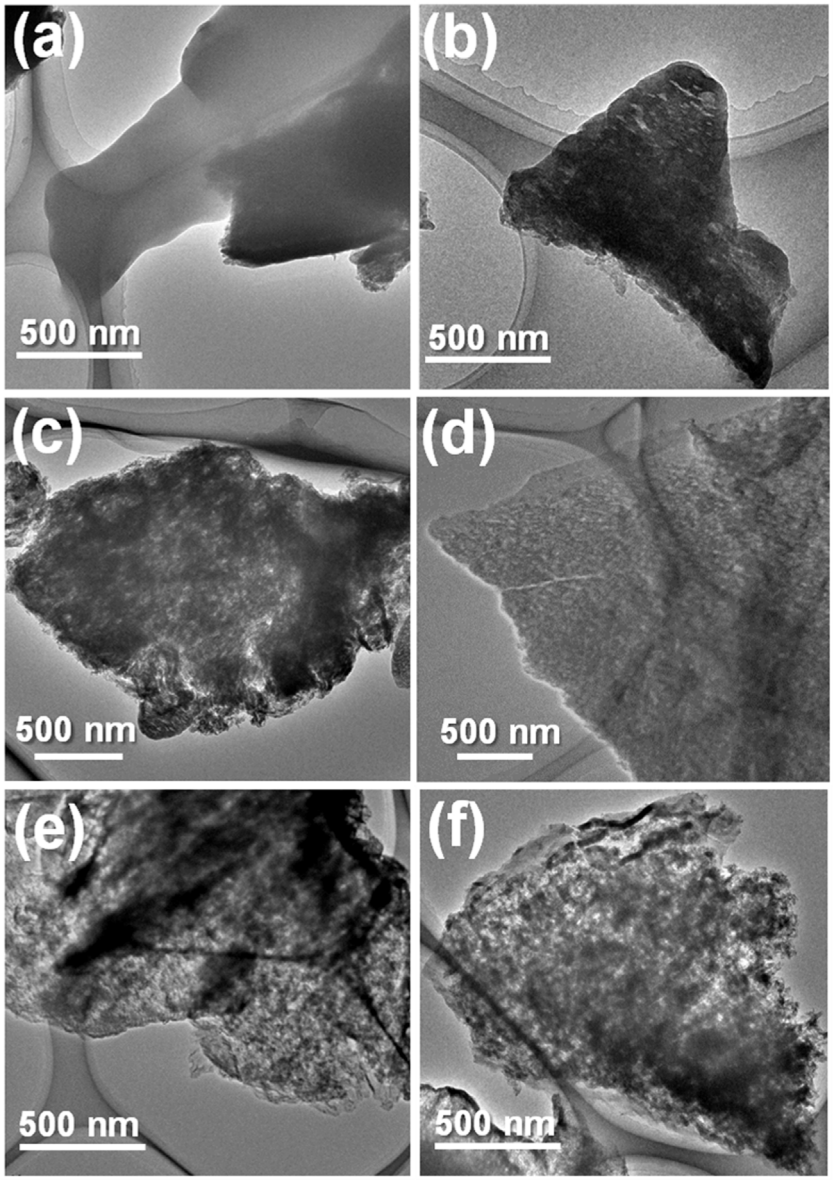

Fig. 2. TEM images of the pristine and the thermally oxidized g-C_3N_4 samples heated in oxygen for 30 min at different temperatures: (a) pristine, (b) 480 °C, (c) 510 °C, (d) 530 °C, (e) 540 °C and (f) 550 °C.

pristine g-C_3N_4 in pure O_2 at a designated temperature will produce more C—O species, as confirmed by the increased intensity of C—O species peak of O XPS spectra (Fig. 4c) and the increased atomic concentration of O (Supplementary Table S1). As the treating temperature increases, the peak intensity at 534.0 eV for the absorbed O_2 decreases and disappeared above 530 °C. This means that the surface of pristine g-C_3N_4 was further oxidized in O_2 and more C—O species were formed without remaining absorbed O_2 on the surface. All the samples exhibit similar N 1 s profiles with core levels at around 397.8, 398.6 and 399.8 eV which can be attributed to sp^2-hybridized aromatic nitrogen atoms bonded to carbon atoms (C=N—C)) [45,46], tertiary nitrogen (N-$(C)_3$) groups linking structural motif (C_6N_7) [7], and amino functional groups (C—N—H) originating from the defective condensation of heptazine substructures [38,41], respectively (Fig. 4d), indicating that this thermal oxidation has little influence on the C—N aromatic systems. XPS and the calculation data manifest that the C/N atomic ratio increases from 0.725 to 0.967 (Table S1), meaning part of N atoms missed during the O_2 treatment. It was reported that the loss of nitrogen in the amine groups was theoretically predicted to be much easier than that in the N(sp^2) and N(sp^3) groups [41]. Therefore, the increased C/N atomic ratio observed could be caused by the partial loss of the amine groups from g-C_3N_4, which is also confirmed by the decreased intensity and slightly increased binding energy of the amino functional groups (C—N—H) in the N 1s spectra of the carbon nitrides (Fig. 4d, Table S2). This suggests that O most probably replaces trace amount of N (amino functional groups) in O_2 treated g-C_3N_4 sample to form C—O bonds. The proposed schematic for the formation of this oxygenated porous g-C_3N_4 by the thermal oxidation method from pristine sample is illustrated in Fig. 5. After thermal oxidation, thermally oxidized g-C_3N_4 with one NH_2 group is replaced by an O atom.

3.3. Chemical bond analysis

FT-IR spectra of the pristine and thermally oxidized g-C_3N_4 obtained from 530 °C samples (Supplementary Fig. S1) provide further molecular structural information. Both the samples appear

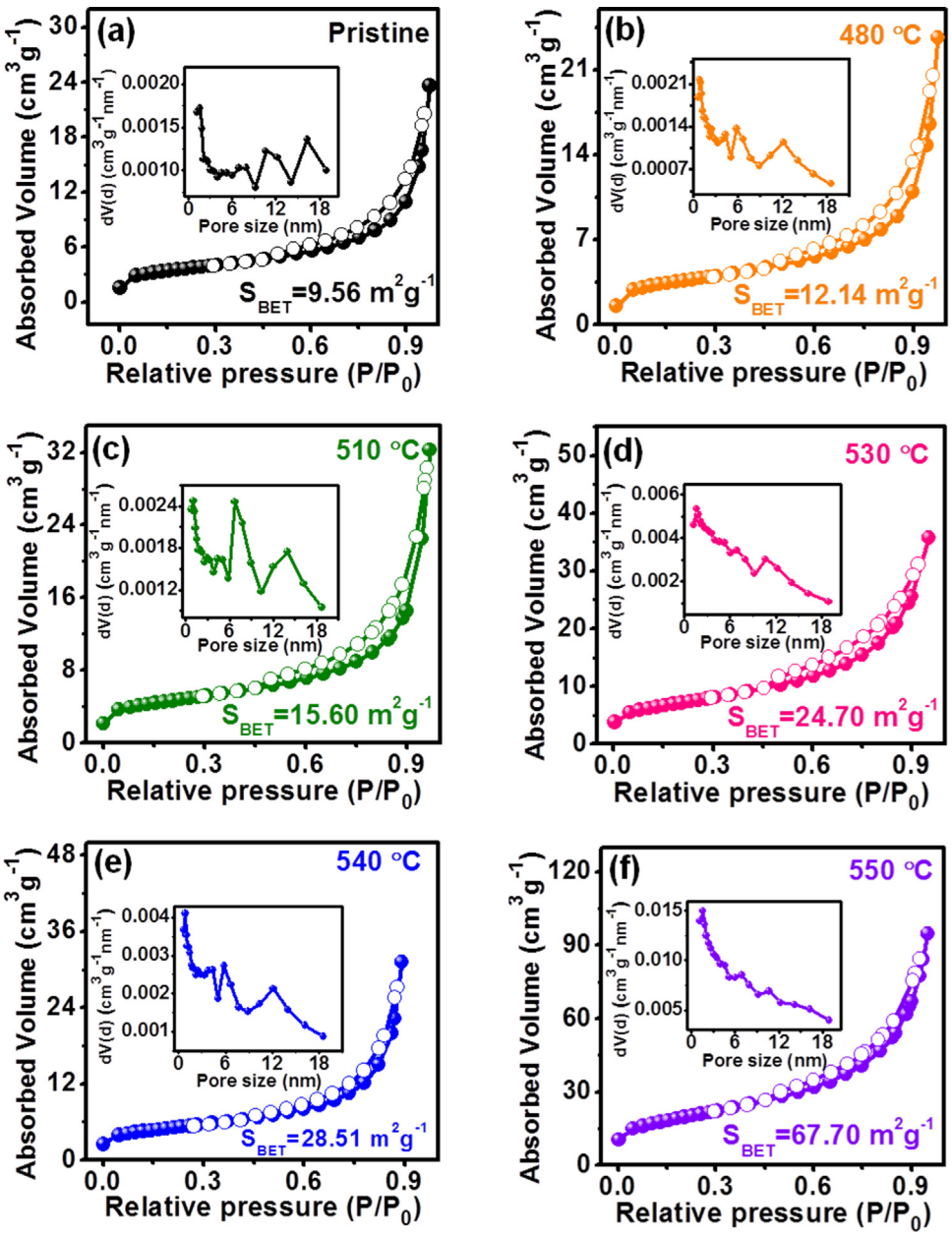

Fig. 3. N_2 adsorption/desorption isotherms and pore size distribution curves of (a) the pristine and the thermally oxidized g-C_3N_4 samples heated in oxygen for 30 min at different temperatures: (b) 480 °C, (c) 510 °C, (d) 530 °C, (e) 540 °C and (f) 550 °C.

the typical FT-IR patterns of g-C_3N_4 [37–41] (Supplementary Fig. S1a). The sharp peak at 807 cm^{-1} observed in the pristine sample is assigned to the typical out-of-plane bending vibration characteristic of the tri-s-triazine unit [37,38,41]. Compared to the 807 cm^{-1} peak in pristine sample, 3 cm^{-1} shift towards high frequencies is observed in the thermally oxidized g-C_3N_4 sample (Supplementary Fig. S1b), predicting that some interactions weakened between the "nitrogen pots" of this g-C_3N_4 sample, probably due to the partial substitution of N atoms by O atoms [41]. Both the pristine and thermally oxidized g-C_3N_4 samples appear typical C=N and C—N heterocycle stretches in 1100–1700 cm^{-1} region [37,38,41], and peaks in this region of the thermally oxidized sample slightly shift to higher wave numbers than the pristine (Supplementary Fig. S1c). It signifies that the C=N and C—N bonds are strengthened due to the introduction of O atoms after thermal oxidation [41]. However, because of the small amount of O atoms in the thermally oxidized g-C_3N_4 and the strongly couple among typical stretching vibration modes of C—C, C—N and C—O bonds [41], the low intensity peaks of C—O species may be covered by aromatic C—N stretching in the modified g-C_3N_4 sample. Hence, the C—O species are difficult to clearly discriminate by FT-IR spectrometer. The broad peak in 3000–3500 cm^{-1} region detected in both samples (Supplementary Fig. S1a) can be attached to N—H stretching vibration mode [34,38,41], declaring that the amino functions still exist in the products after this thermal oxidation. The FTIR spectra further demonstrate that the core chemical structure of the thermally oxidized g-C_3N_4 units is maintained.

3.4. Crystal structure and electronic properties

Crystal structure of the pristine and thermally oxidized g-C_3N_4 samples are recorded by X-ray diffraction (XRD). As illustrated in Fig. 6a, all the thermally oxidized g-C_3N_4 samples show two diffraction peaks of 100 and 002, which is consistent with the pristine

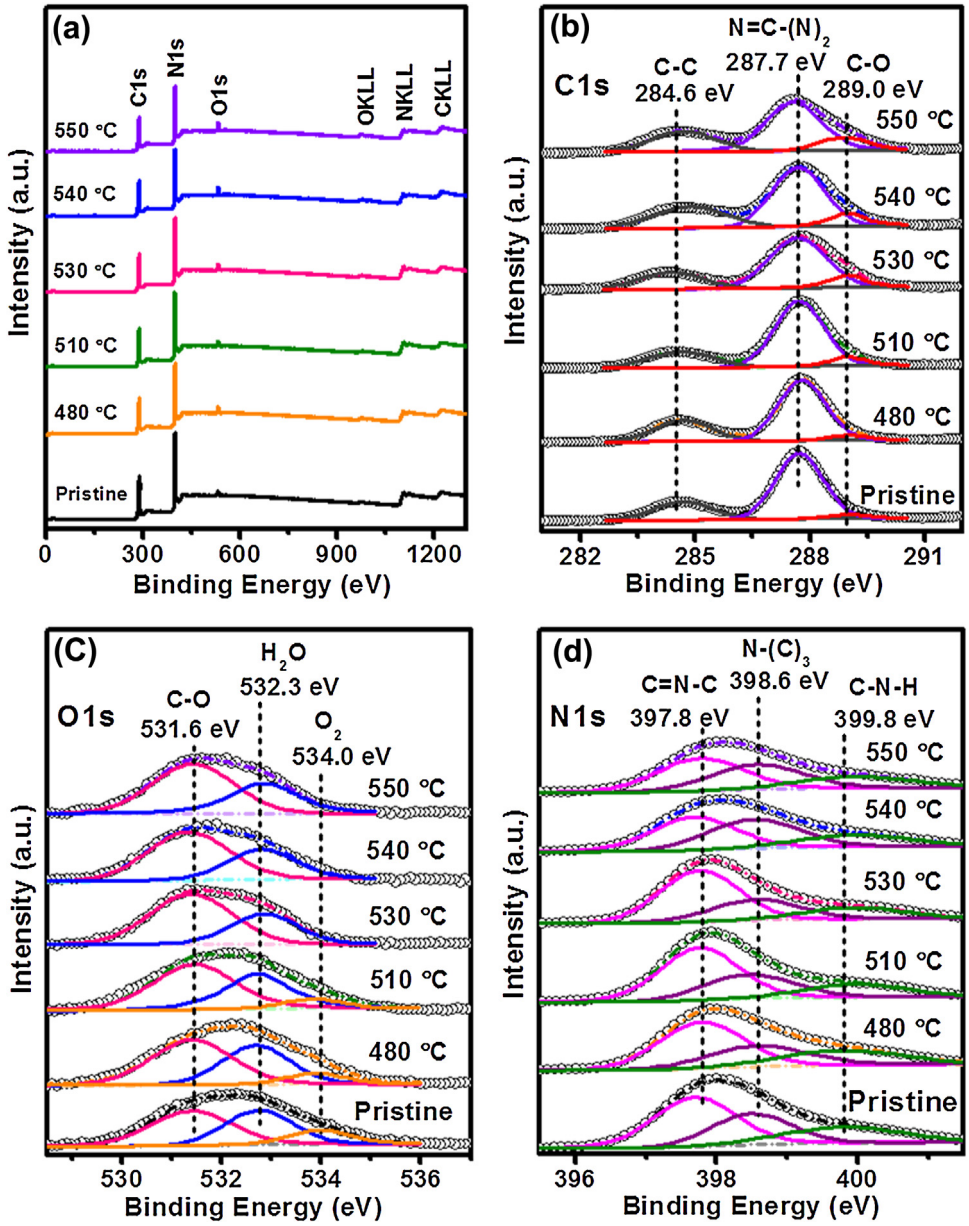

Fig. 4. (a) XPS survey spectra, (b) C 1s, (c) O 1 s and (d) N 1 s high-resolutions of the pristine and the thermally oxidized (heated at 480, 510, 530, 540 and 550 °C in oxygen for 30 min) g-C_3N_4 samples.

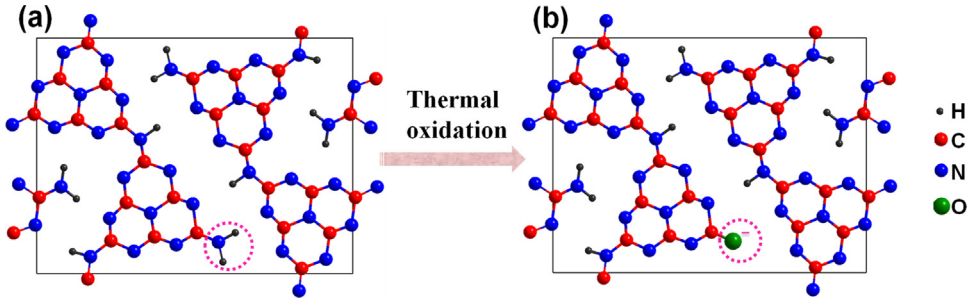

Fig. 5. Schematic for the formation of the porous g-C_3N_4 by the thermal oxidation method: (a) the pristine g-C_3N_4 before thermal oxidation and (b) the thermally oxidized porous g-C_3N_4 with one NH_2 group (in dotted circle in (a)) displaced by an O atom (in dotted circle in (b)).

sample. It proves that the crystal structure of g-C_3N_4 is largely retained after the thermal oxidation process. Those two diffraction peaks of 100 and 002 are attributed to the in-plane repeating unites of the continuous heptazine framework and the stacking of the conjugated aromatic structure of g-C_3N_4, respectively [37–41]. The 100 peaks of the thermally oxidized samples exhibit slight blue

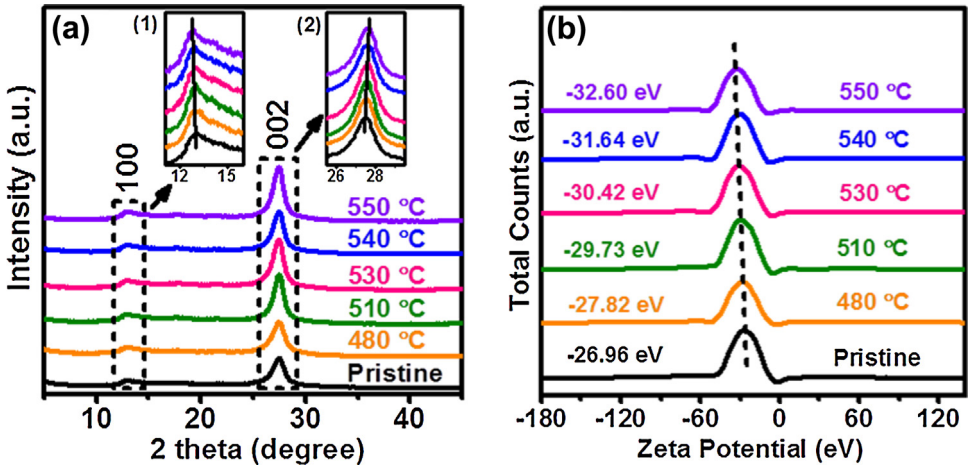

Fig. 6. (a) XRD spectra of the pristine and the thermally oxidized g-C_3N_4 samples heated in oxygen at different temperatures, and the inset images are the corresponding magnified image from the black dotted boxes. (b) Zeta potential distribution curves of the pristine and the thermally oxidized g-C_3N_4 samples.

shift with the increase of temperature, and decrease from 12.90° of the pristine to 12.70° of 550 °C, corresponding to the increase in the distance of in-planar nitride pores from 0.6857 to 0.6965 nm according to Scherrer Equation. Meanwhile, the 002 peaks of the thermally oxidized samples exhibit slight red shift with the increase of temperature, and increase from 27.48° of the pristine to 27.66° of 550 °C, corresponding to a decrease in the interplanar stacking distance from 0.3243 to 0.3222 nm (Supplementary Table S3). This feature could be interpreted as the introduction of oxygen heteroatoms and the consequential disturbance of graphitic structure. When an O atom is inserted into the framework to replace an amine group, one electron form covalent bond with a C atom to form a C—O group and the remaining electron of the O atom delocalizes into the π-conjugated triazine ring, thus creating an electron-rich state of the thermally oxidized g-C_3N_4 (Fig. 5b). Zeta potential distribution curves of the samples dispersed in water indicate that the thermally oxidized g-C_3N_4 samples are more negatively charged than the pristine sample (Fig. 6b). This shows that the incorporation of the O atom has changed the electronic property of the pristine g-C_3N_4, resulting in an electron-rich state of the thermally oxidized g-C_3N_4. The shortened interplanar distance derived from XRD results could be ascribed to the strengthened interactions between the g-C_3N_4 layers caused by higher electronegative doped oxygen atoms in the framework than the substituted nitrogen atoms.

3.5. UV–vis absorption and band structure analysis

The electronic structures and photoelectric properties of the samples are investigated. The UV–vis DRS spectra (Fig. 7a) indicates that the absorption edge of the thermally oxidized porous g-C_3N_4 display a remarkable red shift in comparison with the pristine sample, which promotes to more visible light harvesting. The corresponding band gaps of the pristine and the thermally oxidized porous g-C_3N_4 samples are 2.73 eV, and 2.71 eV at 480 °C, 2.68 eV at 510 °C, 2.63 eV at 530 °C, 2.61 eV at 540 °C and 2.58 eV at 550 °C, respectively (Fig. 7a, inset 1). The red shift of the absorption edge of the thermally oxidized porous g-C_3N_4 can be well explained as a consequence of the changed electronic and microscopic structure by the partial substitution of the N atoms by O atoms demonstrated above. Furthermore, broader and stronger absorption tails, starting at ≈520 nm and extending to 700 nm, are also clearly observed for thermally oxidized porous g-C_3N_4 samples (Fig. 7a, inset 2). The increased optical absorption is related to the excitation from band tails/localized states, originating from the incomplete long-range ordering of atomic structures [23]. Increasing the thermal treatment temperature leads to a gradually increased band-tail related absorption, indicating that higher density of band tails/localized states can be created at a higher temperature. The gradual destruction of the intralayer long-range atomic order of carbon nitride accompanying with the loss of partial nitrogen atoms by the partial substitution of the N atoms by O atoms increases both the density and distribution of band tails/localized states, which is responsible for the increased visible light absorption.

To further investigate the influence of oxygen-containing functional groups on the relative positions of the conduction band minimum (CBM) and valence band maximum (VBM) of the samples, valence band X-ray photoelectron spectroscopy (VB-XPS) and Mott–Schottky plots were employed to determine the electronic structure. Fig. 7b indicates that the VBM of the pristine and thermally oxidized porous g-C_3N_4 are located at 1.26 eV, 1.20 eV, 1.15 eV, 1.05 eV, 1.02 eV, and 0.96 eV, respectively. It means that the VBM of the g-C_3N_4 is disturbed by the thermal oxidation process and the thermally oxidized porous g-C_3N_4 exhibits higher VBM than the pristine. Meanwhile, a significant change in the intrinsic electron distribution in the CB is also achieved for the thermally oxidized porous g-C_3N_4 sample. Combined with the UV–vis DRS result, it can be calculated that the thermally oxidized porous g-C_3N_4 exhibits higher CBM than the pristine, which indicates that the stronger redox ability is realized in the thermally oxidized porous g-C_3N_4. Since an O atom owns one more valence electron than an N atom, the substitution of N sites by O atoms would produce extra electrons in the thermally oxidized porous g-C_3N_4 sample. Subsequently, the extra electrons would be redistributed to their nearest C atoms and delocalized among the big π bonds of the g-C_3N_4, leading to the increased unpaired electrons on the carbon atoms of the aromatic rings, which can be confirmed by the electron spin resonance (ESR) measurement. As evidenced in Fig. 7c, all the samples exhibit an ESR signal with a g value of 2.003, which is attributed to an unpaired electron on the carbon atoms of the aromatic rings within π-bonded nanosized clusters. Compared to pristine g-C_3N_4, the largely stronger spin intensity of the thermally oxidized porous g-C_3N_4 gives evidence for the promoted formation of unpaired electrons [49]. The flat-band potentials of samples were measured using the electrochemical method and the Mott-Schottky plots (Supplementary Fig. S2). The positive slopes of the linear plots apparently disclose the typical n-type characteristic inorganic semiconductors [50], and the conduction band (CB) potential of the samples can be obtained from the intercept on the

abscissa of MS plots. The schematic energy level diagrams of the pristine and the thermally oxidized g-C_3N_4 samples prepared at different temperatures are shown in Fig. 8. It can be seen that CB potential of the thermally oxidized g-C_3N_4 samples increase with the increase of temperature and all are more negative than that of the pristine g-C_3N_4. The higher position of CB will result in stronger reducibility, which may be beneficial for photocatalytic hydrogen generation.

3.6. Optical and photoelectrochemical properties

Fig. 9a reveals the PL spectra of the pristine and thermally oxidized porous g-C_3N_4. As it could be seen from the PL spectra, the treatment of the pristine sample in O_2 leads to substantial suppression of radiative electron–hole recombination in carbon nitrides, as indicated by the greatly weakened PL peaks. For the pristine g-C_3N_4, the PL spectrum emerges a strong emission peak at 456 nm, which is originated from the band-to-band recombination of electrons and holes. The intensity of this band-to-band emission peak decreased dramatically upon the treatment of O_2, which mean that the band-to-band recombination of electrons and holes was effectively inhibited. Moreover, the emission peak experiences a gradual red-shift from the pristine 456 nm to around 466 nm at 550 °C, which is also consistent with the extension of the absorption edge toward long wavelength (Fig. 7a). To gain a quantitative knowledge of the photo-generated charge carrier lifetime in all the samples, the time-resolved PL spectra were investigated and displayed in Fig. 9b, which were monitored at the wavelength of the emission peak of each sample. By the multi-exponential fitting, the average lifetimes of the samples are calculated and presented in Fig. 9b. The average PL lifetime increased with the increase of treating temperature, from 7.81 ns of the pristine g-C_3N_4 to 10.80 ns of the product obtained at the critical temperature at 530 °C. The elongating of the PL lifetime and related suppression of the band-to-band recombination of electrons and holes after O_2 treatment below 530 °C indicated that the charge separation efficiency was increased, which is beneficial for the photocatalytic reactions [51]. However, further increasing the temperature to 540 °C and 550 °C leads to a dramatical decrease of the average PL lifetime, and it reaches 5.57 ns and 4.44 ns, respectively. The remarkable shortening of the PL lifetime and related suppression of the band-to-band recombination of electrons and holes is attributed to the emergence of the band-tails-involved rapid radiative electron–hole recombination processes in g-C_3N_4 after O_2 treatment above 540 °C. As shown in Fig. 7a, the band-tail related absorption band has a gradually increased absorbance with the increase of treatment temperature, which would increase the density of band tails/localized states. The high density of band tails/localized states induced by O_2 treatment above 540 °C can act as shallow trap states of photogenerated charge carriers, leading to a remarkable shortening of the PL lifetime and a weakening of PL intensity. For a combined analysis of the photogenerated charge separation and transfer performance of the samples, photocurrent was evaluated. Fig. 9c displays that the photocurrent of g-C_3N_4 increases with the increase of temperature to a plateau at 530 °C under visible light irradiation, confirming the constructive effect in improving charge mobility and separation after this thermal oxidation [52]. However, the photocurrent decreases when the temperature increases to 540 °C and 550 °C, indicating that the formed high density of band tails/localized states would trap the photogenerated charge carriers, which significantly inhibited the transition of charge carriers to surface of g-C_3N_4. Based on the above discussion, an electronic excitation and transition mechanism of g-C_3N_4 before and after O_2 treatment was illustrated in Fig. S3.

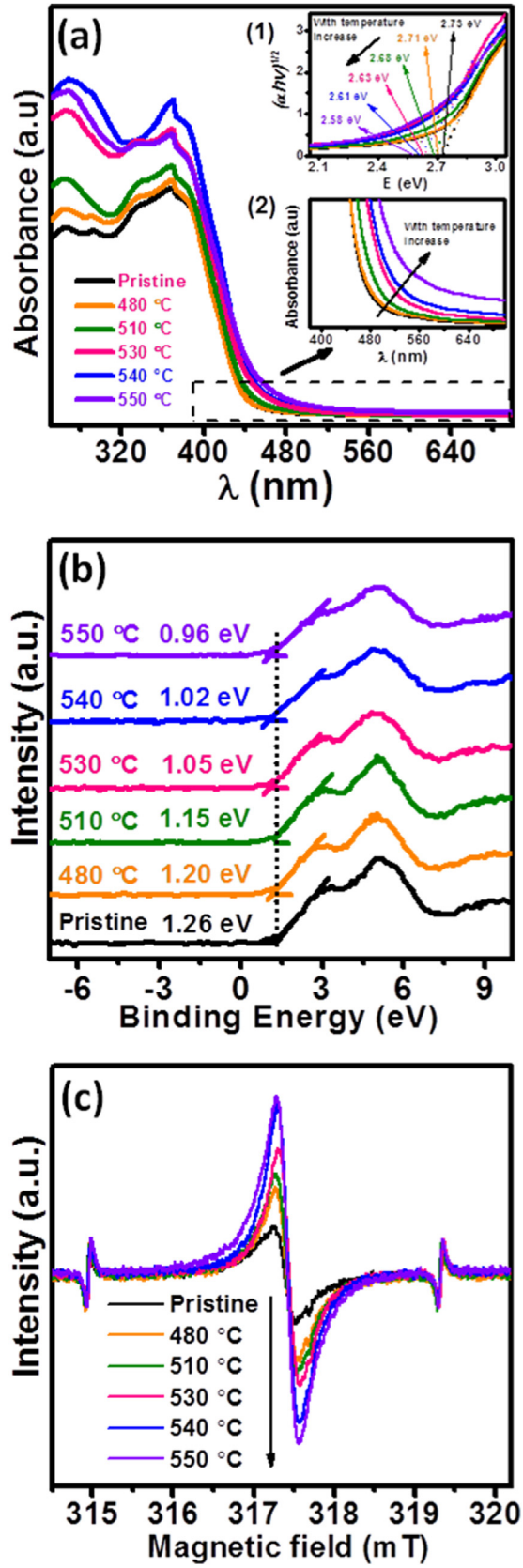

Fig. 7. (a) UV–vis diffuse reflectance spectroscopy spectra, (b) high resolution valence band XPS spectra, and (c) electron spin resonance (ESR) signals of the pristine and the thermally oxidized g-C_3N_4 samples heated at different temperatures. The inset images in (a) are: (1) the calculated band gaps and (2) the corresponding magnified image from the black dotted boxes.

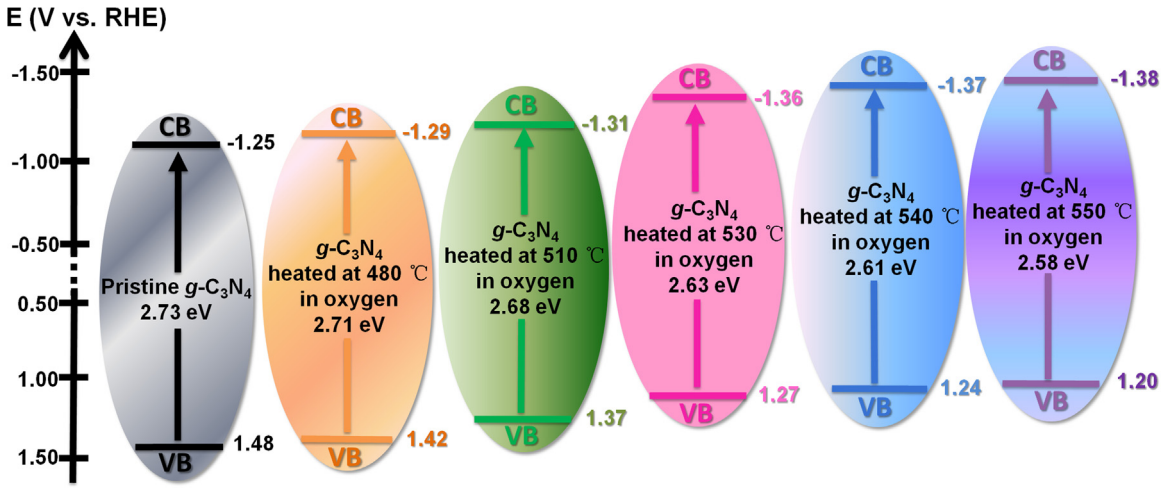

Fig. 8. Schematic energy level diagrams of the pristine and the thermally oxidized g-C_3N_4 samples heated in oxygen for 30 min at different temperatures.

3.7. Photocatalytic performance evaluation

The photocatalytic performance of the samples was evaluated by photocatalytic hydrogen generation, which was performed in an aqueous solution containing triethanolamine as an electron donor, and 3 wt% Pt as co-catalyst under visible light irradiation (Fig. 10a). The highest photocatalytic hydrogen evolution activity of the thermally oxidized porous g-C_3N_4 sample is 1430.1 μmol g^{-1} h^{-1} in 8 h under visible light irradiation, which is 4.3 times as high as that of the pristine g-C_3N_4 (334.3 μmol g^{-1} h^{-1}). The relationship between temperature and the corresponding photocatalytic H_2 evolution is displayed in Fig. 10b. It can be seen that all the oxygen treated samples display enhanced photocatalytic hydrogen evolution activity than the pristine sample. The photocatalytic H_2 evolution rate of the samples increases with increasing temperatures up to 530 °C. Further increasing the temperature to 540 or 550 °C gives rise to decreased activities but they are still superior to the pristine sample. The activity decreases beyond 530 °C is probably because of the formation of the high density of band tails/localized states in g-C_3N_4 after O_2 treatment above 540 °C that would trap the charge carriers, which significantly inhibited the transition of charge carriers to surface for the desired redox reactions. Moreover, the collapse of pore walls would also lead to the decreased activities [23]. The stability of photocatalytic hydrogen evolution for three cycles under the same reaction conditions indicating the good photocatalytic stability of the thermally oxidized porous g-C_3N_4 (Fig. 10c). Moreover, the XRD pattern of the thermally oxidized porous g-C_3N_4 after three cycles of photocatalytic H_2 evolution was recorded, which further confirm its good stability (Supplementary Fig. S4). In order to further prove the superiority of O_2 treated g-C_3N_4 (thermally oxidized sample) for photocatalytic application, the Ar treated g-C_3N_4 (non-oxidized sample) was also prepared under the same temperature condition (see See experimental procedures). As shown in Supplementary Fig. S5a, the Ar treated sample also shows porous structure because of the selective breaking of hydrogen bonds in g-C_3N_4 [23]. The N_2 adsorption-desorption isotherms show that the S_{BET} of the Ar treated sample is about 20.28 m^2 g^{-1}, which is similar to the oxygen treated sample (Supplementary Fig. S5). Fig. S5e shows the photocatalytic H_2 evolution performances of the pristine g-C_3N_4, the O_2 treated g-C_3N_4 and the Ar treated g-C_3N_4, respectively. It is apparent that the O_2 treated g-C_3N_4 displays much higher photocatalytic H_2 evolution activity than the Ar treated sample, revealing that the introduction of functional C—O species in the intralayer framework of g-C_3N_4 through oxidation in O_2 plays a more important role in the enhanced photocatalysis. To the best of our knowledge, the photocatalytic hydrogen evolution rate is much higher than some previously reported modified g-C_3N_4 photocatalysts under visible light as listed in Supplementary Fig. S6. The notable photocatalytic hydrogen evolution enhancement in the thermally oxidized porous g-C_3N_4 heated at 530 °C can be interpreted by the following reasons. Firstly, the larger surface area of the thermally oxidized porous g-C_3N_4 leads to more surface reaction sites for the photocatalytic H_2 evolution compared to the pristine. Secondly, the partial substitution of N atoms by O atoms in the intralayer framework of g-C_3N_4 through thermal oxidation in O_2 not only extends light absorption range for effective use of more visible light but also suppresses the radiative electron–hole recombination, which plays a more important role in the improvement of photocatalytic H_2 evolution reaction. In addition to these electronic structure-induced favourable features, the abundant interconnected pores through the porous structure simultaneously formed by the oxygen etching can geometrically shorten the diffusion lengths of both the photoexcited electrons from the interior to edges of the layers and reactants from the surface to the interior of a particle along the interlayer galleries, which also favours photocatalytic reaction by lowering the bulk recombination probability of electrons and holes, and also promoting mass transport. Additionally, the up-shifted conduction band of thermally oxidized g-C_3N_4 displays stronger reducibility which is also in favour of photocatalytic hydrogen evolution.

4. Conclusions

In summary, thermally oxidized porous g-C_3N_4 is obtained by a facile oxidation approach. The photocatalytic hydrogen production of modified g-C_3N_4 presents 4.3 times as high as that of the pristine sample in 8 h under visible-light irradiation due to the synergistic effects of the extended visible light response, up-shifted conduction band, improved separation efficiency of the photoinduced charge carriers, and the enlarged specific surface area. What's more, we found that the O_2 treated g-C_3N_4 displays much higher photocatalytic H_2 evolution activity than the Ar treated sample prepared under the same temperature condition, indicating the superiority of thermally oxidized property for photocatalytic application. This study demonstrates that the thermal oxidation modification is a cost-effective approach for the mass production of porous g-C_3N_4, and therefore it has great potentials in modifying tailored oxidized porous g-C_3N_4 for optoelectronics and photocatalytic applications.

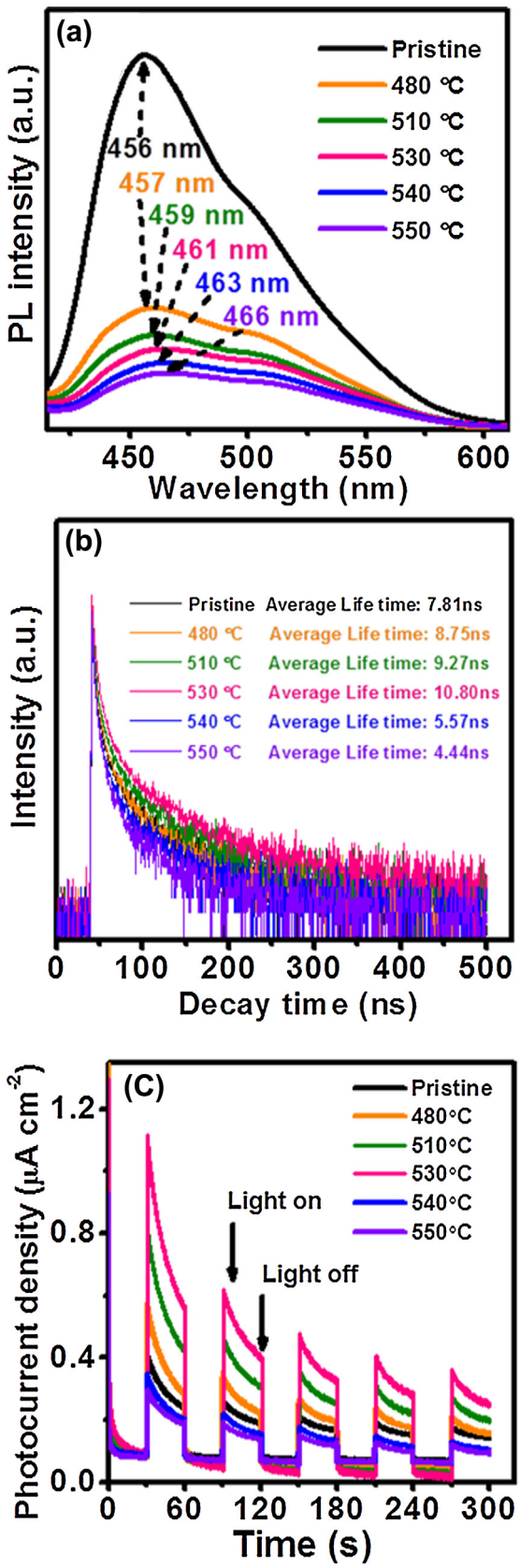

Fig. 9. (a) Photoluminescence spectra, (b) Time-resolved fluorescence spectra, and (c) time dependent photocurrent spectra of the pristine and the thermally oxidized g-C_3N_4 samples heated in oxygen for 30 min at different temperatures.

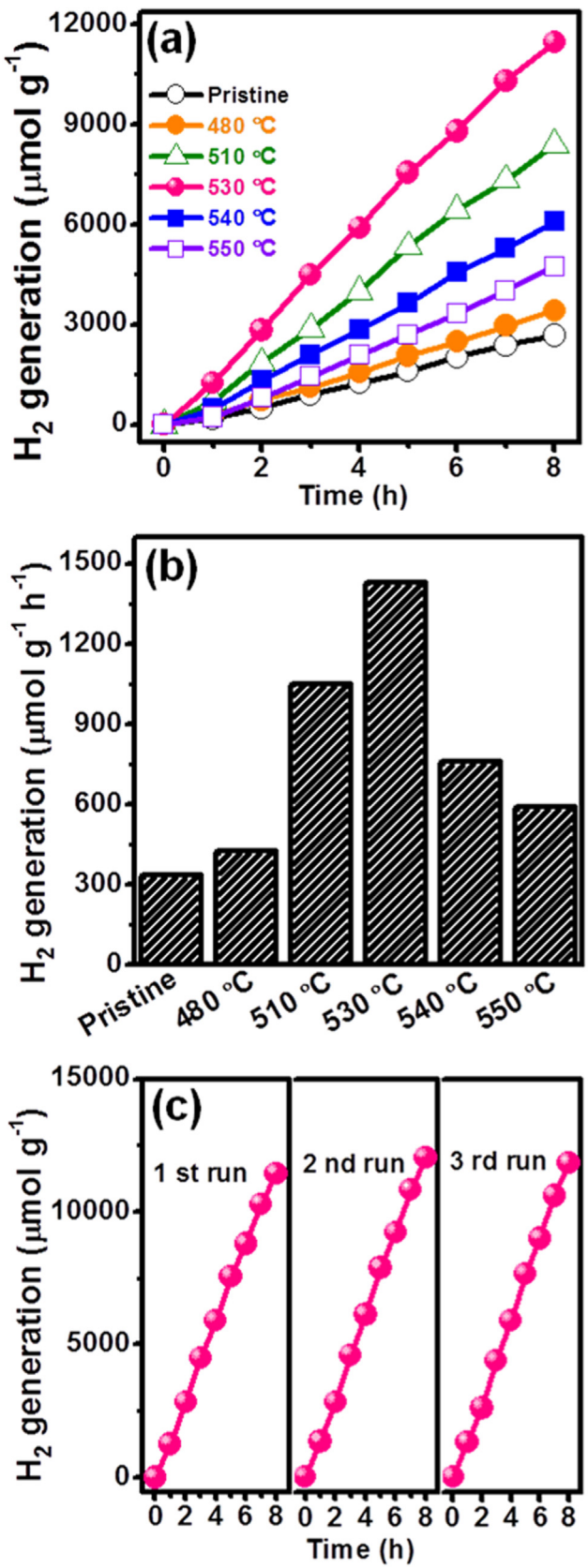

Fig. 10. (a) Time dependent photocatalytic H_2 evolution over the pristine and the thermally oxidized g-C_3N_4 samples under visible light irradiation, (b) corresponding relationship between the treatment temperatures and the photocatalytic H_2 evolution rates. (c) Photocatalytic hydrogen evolution cycle performance of the thermally oxidized g-C_3N_4 prepared at 530 °C.

Acknowledgements

The authors thank to World Premier International Research Center Initiative on Materials Nanoarchitectonics (WPI-MANA), National Basic Research Program of China (973 Program, 2014CB239301), the National Natural Science Foundation of China (No. 51472152), Natural Science Foundation of Shaanxi province (No. 2015JM5251), Scientific Research Project of Education Department of Shaanxi Province (No. 15JK1072), Innovation Team Assistance Foundation of Shaanxi Province (No. 2013KCT-06), State Scholarship Fund by China Scholarship Council (CSC) in 2015 and the Graduate Innovation Foundation of Shaanxi University of Science and Technology.

Appendix A. Supplementary data

Supplementary data associated with this article can be found, in the online version, at http://dx.doi.org/10.1016/j.apcatb.2016.11.047.

References

[1] J. Liu, H. Wang, M. Antonietti, Chem. Soc. Rev. 45 (2016) 2308–2326.
[2] L. Lin, H. Ou, Y. Zhang, X. Wang, ACS Catal. 6 (2016) 3921–3931.
[3] X. Wang, S. Blechert, M. Antonietti, ACS Catal. 2 (2012) 1596–1606.
[4] S. Cao, J. Yu, J. Phys. Chem. Lett. 5 (2014) 2101–2107.
[5] X. Wang, K. Maeda, A. Thomas, K. Takanabe, G. Xin, J.M. Carlsson, K. Domen, M. Antonietti, Nat. Mater. 8 (2009) 76–80.
[6] S. Cao, J. Low, J. Yu, M. Jaroniec, Adv. Mater. 27 (2015) 2150–2176.
[7] W.J. Ong, L.L. Tan, Y.H. Ng, S.T. Yong, S.P. Chai, Chem. Rev. 116 (2016) 7159–7329.
[8] J. Zhang, M. Zhang, L. Lin, X. Wang, Angew. Chem. Int. Ed. 54 (2015) 6297–6301.
[9] Y. Zhang, A. Thomas, M. Antonietti, X. Wang, J. Am. Chem. Soc. 131 (2009) 50–51.
[10] C. Pan, J. Xu, Y. Wang, D. Li, Y. Zhu, Adv. Funct. Mater. 22 (2012) 1518–1524.
[11] H. Li, S. Gan, H. Wang, D. Han, L. Niu, Adv. Mater. 27 (2015) 6906–6913.
[12] H. Wu, D. Chen, N. Li, Q. Xu, H. Li, J. He, J. Lu, Nanoscale 8 (2016) 12066–12072.
[13] X. Song, Y. Hu, M. Zheng, C. Wei, Appl. Catal. B: Environ. 182 (2016) 587–597.
[14] W.J. Ong, L.L. Tan, S.P. Chai, S.T. Yong, A.R. Mohamed, Nano Energy 13 (2015) 757–770.
[15] L. Shi, T. Wang, H. Zhang, K. Chang, J. Ye, Adv. Funct. Mater. 25 (2015) 5360–5367.
[16] K. Wang, Q. Li, B. Liu, B. Cheng, W. Ho, J. Yu, Appl. Catal. B: Environ. 176 (2015) 44–52.
[17] H.J. Kong, D.H. Won, J. Kim, S.I. Woo, Chem. Mater. 28 (2016) 1318–1324.
[18] G. Zhang, C. Huang, X. Wang, Small 11 (2015) 1215–1221.
[19] C. Ye, J.X. Li, Z.J. Li, X.B. Li, X.B. Fan, L.P. Zhang, B. Chen, C.H. Tung, L.Z. Wu, ACS Catal. 5 (2015) 6973–6979.
[20] Q. Han, B. Wang, Y. Zhao, C. Hu, L. Qu, Angew. Chem. Int. Ed. 54 (2015) 11433–11437.
[21] Q. Han, B. Wang, J. Gao, Z. Cheng, Y. Zhao, Z. Zhang, L. Qu, ACS Nano 10 (2016) 2745–2751.
[22] L. Shi, K. Chang, H. Zhang, X. Hai, L. Yang, T. Wang, J. Ye, Small 12 (2016) 4431–4439.
[23] Y. Kang, Y. Yang, L.C. Yin, X. Kang, L. Wang, G. Liu, H.M. Cheng, Adv. Mater. 28 (2016) 6471–6477.
[24] X. Yue, S. Yi, R. Wang, Z. Zhang, S. Qiu, Sci. Rep. 6 (2016) 22268.
[25] H. Yu, F. Chen, F. Chen, X. Wang, Appl. Surf. Sci. 358 (2015) 385–392.
[26] Q. Gu, J. Liu, Z. Gao, C. Xue, Chem. Asian J. (2016), http://dx.doi.org/10.1002/asia.201601201.
[27] J. Fang, H. Fan, M. Li, C. Long, J. Mater. Chem. A 3 (2015) 13819–13826.
[28] G. Liu, P. Liu, C. Sun, S.C. Smith, Z. Chen, G.Q. Lu, H.M. Cheng, J. Am. Chem. Soc. 132 (2010) 11642–11648.
[29] C. Lu, P. Zhang, S. Jiang, X. Wu, S. Song, M. Zhu, Z. Luo, Z. Li, F. Liu, Y. Liu, Y. Wang, Z. Le, Appl. Catal. B: Environ. 200 (2017) 378–385.
[30] C. Lu, R. Chen, X. Wu, M. Fan, Y. Liu, Z. Le, S. Jiang, S. Song, Appl. Surf. Sci. 360 (2016) 1016–1022.
[31] S. Guo, Z. Deng, M. Li, B. Jiang, C. Tian, Q. Pan, H. Fu, Angew. Chem. Int. Ed. 55 (2016) 1830–1834.
[32] Y. Kang, Y. Yang, L. Yin, X. Kang, G. Liu, H. Cheng, Adv. Mater. 27 (2015) 4572–4577.
[33] J. Ran, T.Y. Ma, G. Gao, X.W. Du, S.Z. Qiao, Energy Environ. Sci. 8 (2015) 3708–3717.
[34] Y. Zhou, L. Zhang, J. Liu, X. Fan, B. Wang, M. Wang, W. Ren, J. Wang, M. Li, J. Shi, J. Mater. Chem. A 3 (2015) 3862–3867.
[35] G. Zhang, M. Zhang, X. Ye, X. Qiu, S. Lin, Adv. Mater. 26 (2014) 805–809.
[36] Q. Han, C. Hu, F. Zhao, Z. Zhang, N. Chen, L. Qu, J. Mater. Chem. A 3 (2015) 4612–4619.
[37] Z.F. Huang, J. Song, L. Pan, Z. Wang, X. Zhang, J.J. Zou, W. Mi, X. Zhang, Nano Energy 12 (2015) 646–656.
[38] S. Guo, Y. Zhu, Y. Yan, Y. Min, J. Fan, Q. Xu, Appl. Catal. B: Environ. 185 (2016) 315–321.
[39] X. She, L. Liu, H. Ji, Z. Mo, Y. Li, L. Huang, D. Du, H. Li, Appl. Catal. B: Environ. 187 (2016) 144–153.
[40] Y. Bu, Z. Chen, Electrochim. Acta 144 (2014) 42–49.
[41] J. Li, B. Shen, Z. Hong, B. Lin, B. Gao, Y. Chen, Chem. Commun. 48 (2012) 12017–12019.
[42] X. She, J. Wu, J. Zhong, H. Xu, Y. Yang, R. Vajtai, J. Lou, Y. Liu, D. Du, H. Li, P.M. Ajayan, Nano Energy 27 (2016) 138–146.
[43] Q. Liang, Z. Li, X. Yu, Z.H. Huang, F. Kang, Q.H. Yang, Adv. Mater. 27 (2015) 4634–4639.
[44] J.C. Groen, L.A.A. Peffer, J. Pérez-Ramírez, Microporous Mesoporous Mater. 60 (2003) 1–17.
[45] W. Yu, D. Xu, T. Peng, J. Mater. Chem. A 3 (2015) 19936–19947.
[46] P. Qiu, H. Chen, C. Xu, N. Zhou, F. Jiang, X. Wang, Y. Fu, J. Mater. Chem. A 3 (2015) 24237–24244.
[47] D.J. Martin, K. Qiu, S.A. Shevlin, A.D. Handoko, X. Chen, Z. Guo, J. Tang, Angew. Chem. Int. Ed. 53 (2014) 9240–9245.
[48] G. Zhang, S. Zang, X. Wang, ACS Catal. 5 (2015) 941–947.
[49] Y. Chen, B. Wang, S. Lin, Y. Zhang, X. Wang, J. Phys. Chem. C 118 (2014) 29981–29989.
[50] L. Yang, J. Huang, L. Cao, L. Shi, Q. Yu, X. Kong, Y. Jie, Sci. Rep. 6 (2016) 27765.
[51] R. Kuriki, H. Matsunaga, T. Nakashima, K. Wada, A. Yamakata, O. Ishitani, K. Maeda, J. Am. Chem. Soc. 138 (2016) 5159–5170.
[52] L. Shi, T. Wang, H. Zhang, K. Chang, X. Meng, H. Liu, J. Ye, Adv. Sci. 2 (2015) 1500006.